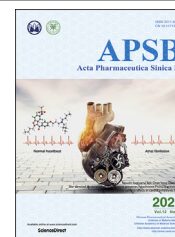




Chinese Pharmaceutical Association
Institute of Materia Medica, Chinese Academy of Medical Sciences

Acta Pharmaceutica Sinica B

www.elsevier.com/locate/apsb
www.sciencedirect.com



ORIGINAL ARTICLE

Ionic co-aggregates (ICAs) based oral drug delivery: Solubilization and permeability improvement



Xianzi Zheng[†], Zhezheng Fang[†], Weizi Huang, Jianping Qi,
Xiaochun Dong, Weili Zhao, Wei Wu^{*}, Yi Lu^{*}

Key Laboratory of Smart Drug Delivery of MOE, School of Pharmacy, Fudan University, Shanghai 201203, China

Received 27 December 2021; received in revised form 26 February 2022; accepted 23 March 2022

KEY WORDS

Ionic co-aggregates;
Molecular dynamics
simulation;
Oral;
Bioavailability;
Aggregation-caused
quenching;
Paclitaxel;
In vivo fate;
Caco-2

Abstract Due to the overwhelming percentage of poorly water-soluble drugs, pharmaceutical industry is in urgent need of efficient approaches for solubilization and permeability improvement. Salts consisting of lipophilic fatty acid anions and hydrophilic choline cations are found to be surface active and able to form ionic co-aggregates (ICAs) in water. Choline oleate-based ICAs significantly enhance oral absorption of paclitaxel (PTX) as compared with cremophor EL-based micelles (MCs). Aggregation-caused quenching probes enable tracking of intact ICAs in *in vivo* transport and cellular interaction. Prolonged intestinal retention of ICAs than MCs implies stronger solubilizing capability *in vivo*. *Ex vivo* imaging of major organs and intestinal tracts suggests transepithelial transport of intact ICAs. Cellular studies support the enhanced absorption of PTX and transmembrane transport of intact ICAs. In conclusion, ICAs, consisting of lipophilic ions and hydrophilic counter-ions, are of great potential in delivery of poorly water-soluble drugs by enhancing solubility and permeability.

© 2022 Chinese Pharmaceutical Association and Institute of Materia Medica, Chinese Academy of Medical Sciences. Production and hosting by Elsevier B.V. This is an open access article under the CC BY-NC-ND license (<http://creativecommons.org/licenses/by-nc-nd/4.0/>).

*Corresponding author. Tel.: +86 21 51980084.

E-mail addresses: wuwei@shmu.edu.cn (Wei Wu), fd_luyi@fudan.edu.cn (Yi Lu).

[†]These authors made equal contributions to this work.

Peer review under responsibility of Chinese Pharmaceutical Association and Institute of Materia Medica, Chinese Academy of Medical Sciences

<https://doi.org/10.1016/j.apsb.2022.04.011>

2211-3835 © 2022 Chinese Pharmaceutical Association and Institute of Materia Medica, Chinese Academy of Medical Sciences. Production and hosting by Elsevier B.V. This is an open access article under the CC BY-NC-ND license (<http://creativecommons.org/licenses/by-nc-nd/4.0/>).

1. Introduction

Solubility and permeability are key determinants for druggability and bioavailability of an active pharmaceutical ingredient (API)¹. Lack of biologically acceptable excipients disables the development of liquid preparations. Albeit the feasibility to form solid dosage forms, poor solubility severely limits the performance of the preparations, because dissolution of an API in the administration site is a prerequisite for its absorption. Even though the APIs are dissolved, the molecules should permeate across biomembranes (e.g., the epithelium, the stratum corneum, and the cornea) for absorption. More than 90% of the candidate APIs and 40% of the marketed ones are poorly soluble in water and, consequently, are plagued with poor druggability and bioavailability^{2–4}. Pharmacists are constantly looking for innovative, biologically acceptable, and highly efficient armamentarium for delivery of poorly soluble drugs.

Surfactants are one of the most widely used excipients in pharmaceuticals to overcome several issues concerning drug delivery, from the poor solubility to the low permeability⁵. Surfactants are amphipathic molecules consisting of a hydrophilic and a hydrophobic group that are covalently connected. They aggregate spontaneously in water and form the micelle structure, which enables solubilization of poorly soluble drugs in the lipophilic. For example, cremophor EL and ethanol was adopted as solvent in Taxol® to dissolve paclitaxel (PTX), which form micelles upon dilution with normal saline. In addition, surfactants are excellent penetration enhancers that improve permeability of drug molecules across various biological barriers^{6,7}. Our previous studies even show permeation of intact micelles across the intestinal epithelia and the nasal mucosa^{8–10}. Nonetheless, it is well recognized that surfactants induce serious allergic reaction. In some cases, premedication is required to prevent the hypersensitivity reactions. Polyethylene glycols (PEGs), the hydrophilic group commonly adopted in surfactant molecules, are recently found to be the culprit that induces the allergic reaction^{11–13}. The situation may be more common than we have recognized^{14,15}.

We recently found that salts consisting of lipophilic ions and hydrophilic counter-ions are surface active. Choline salts of fatty acid ([Ch][FA]) are one of the typical instances, which are completely dissolved in water to form colloidal solution at room temperature. Although alkali salts of higher fatty acids are the oldest and most common surfactants, they cannot form clear micellar solution due to hydrolysis in water. For example, sodium oleate is partially hydrolyzed in water, leading to a production of oleic acid and a milky solution. We infer that choline cations co-aggregate with fatty acid anions in aqueous solution to form ionic co-aggregates (ICAs). The bulky quaternary ammonium head-group of choline may be critical to the integrity of ICAs. Of note is that [Ch][FA] is different to ionic surfactants, because the surface activity of the latter is mainly originated from the amphiphilic cations or anions. The amphiphilic ions alone can form micelles without the aids of the counter ions. Besides choline and fatty acids, ICAs may be constructed by the combination of lipophilic ions and hydrophilic counter-ions. In this sense, ICAs stand for a preferable strategy for delivery of poorly soluble drugs. The salt formation is far more convenient than chemical synthesis, while side effects associating with PEG may be avoided. The huge library of ions enables virtually unlimited combinations of cations and anions for screening. The micelle-like structure endows ICAs with solubilizing and permeability enhancing capability, which are

critical attributes in the delivery of poorly water-soluble APIs *via* different routes. Since oral administration is the most convenient but challenging route, we prefer validating the enhanced oral absorption of ICAs firstly in the proof-of-concept study.

Fig. 1 shows the idea of the study. [Ch][FA] are synthesized by metathesis reaction, which spontaneously form ICAs in water. The aggregation-caused quenching (ACQ) probes enable discrimination of intact ICAs from free probes, because the probes emit strong near infrared region (NIR) fluorescence in molecular dispersion, but are quenched in aggregation state upon contacting with water^{16,17}. Therefore, the critical aggregation concentrations (CACs) of the [Ch][FA] are measured by the indication of the ACQ fluorescence. Molecular dynamics simulation reveals the dynamic co-aggregation of choline oleate ([Ch][Ole]) in water. The enhanced oral bioavailability of [Ch][Ole]-based ICAs is validated with a model drug—PTX. More importantly, the *in vivo* transport of intact ICAs is traced *via* the ACQ probes to understand the underlying mechanisms for enhanced oral absorption.

2. Materials and methods

2.1. Materials

The ACQ probes, P2 ($\lambda_{\text{abs}}/\lambda_{\text{em}} = 708 \text{ nm}/732 \text{ nm}$) and P4 ($\lambda_{\text{abs}}/\lambda_{\text{em}} = 651 \text{ nm}/662 \text{ nm}$), were synthesized in the lab. Oleic acid, decanoic acid, lauric acid, myristic acid, palmitic acid, and stearic acid were purchased from Sinopharm Reagent Co., Ltd. (Shanghai, China). Cremophor EL, choline hydroxide, linoleic acid, and linolenic acid were obtained from Aladdin Biochemical Technology Co., Ltd. (Shanghai, China). Paclitaxel and docetaxel were from Meilun Biotechnology Co., Ltd. (Dalian, China). Diamidino-2-phenylindole (DAPI) for nuclear staining was purchased from Yeasen Biotech Co., Ltd. (Shanghai, China). Caco-2 and Raji cells were from National Collection of Authenticated Cell Cultures (Shanghai, China), while HT29-MTX cells were from China Center for Type Culture Collection (Wuhan, China).

2.2. Animals

Male Sprague–Dawley (SD) rats, $180 \pm 20 \text{ g}$, were obtained from Shanghai SLAC Laboratory Animal Co., Ltd. (Shanghai, China). The animal research protocol (2021-03-YJ-LY-11) was approved by the Institutional Animal Care and Use Committee at School of Pharmacy, Fudan University. The team fully complied with international guidelines on animal welfare.

2.3. Synthesis of [Ch][FA]

Metathesis reaction was adopted to synthesize [Ch][FA]. Briefly, equimolar (0.01 mol) choline hydroxide and fatty acid was dissolved in 2 mL ethanol and mixed thoroughly. The solution was stirred by magnetic stirrer at 500 rpm (RCT basic, IKA, Staufen, Germany) for 24 h. The mixture was then concentrated *via* rotary evaporation (RV10, IKA, Staufen, Germany) at $60 \text{ }^\circ\text{C}$ for 2 h, followed by a vacuum drying ($60 \text{ }^\circ\text{C}$) for 48 h.

2.4. Characterization of [Ch][FA]

[Ch][FA] was characterized by ^1H NMR (nuclear magnetic resonance) spectroscopy measurements. The salts were dissolved in

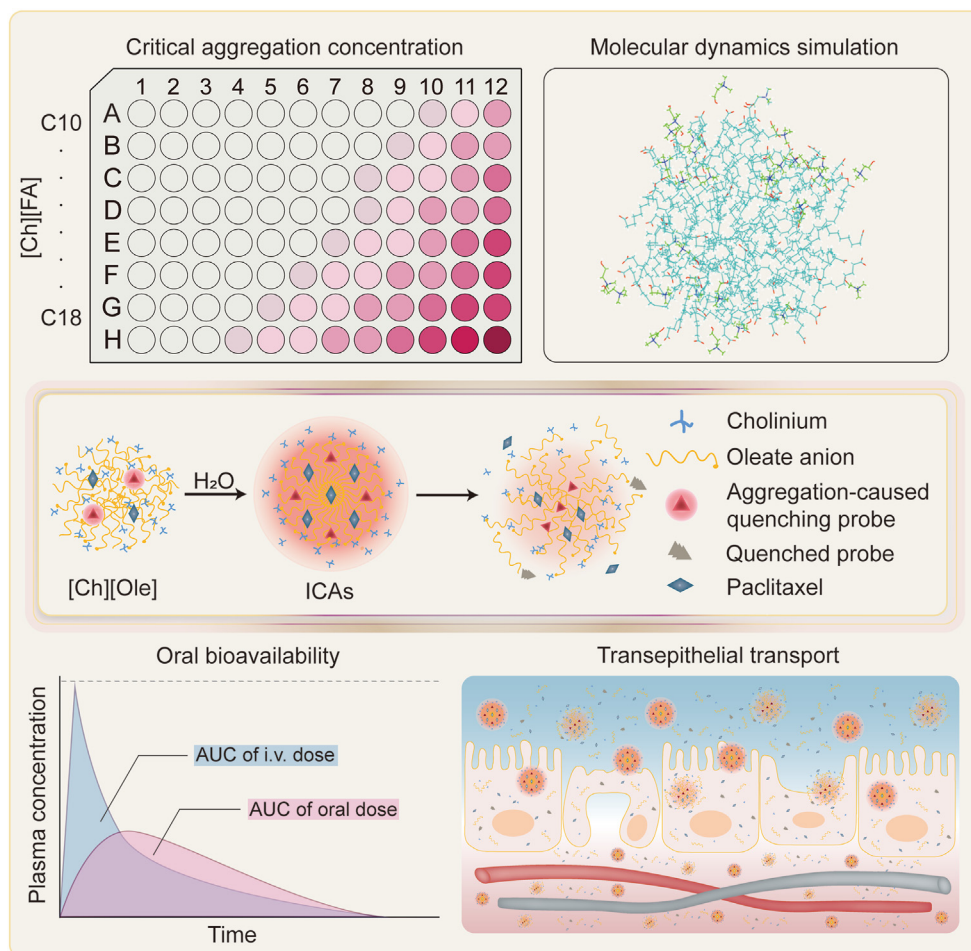


Figure 1 Schematic representation for the understanding of aggregation behavior of [Ch][FA] in water and the enhanced absorption of paclitaxel from [Ch][Ole]-based ICAs.

deuterated DMSO (20 mg/mL) with tetramethylsilane as the internal standard. ^1H NMR spectra of raw materials and the salts were recorded by 400 MHz NMR spectrometer (Varian, Palo Alto, CA, USA). A Nicolet Avatar 360 spectrometer (Madison, WI, USA) was used for measurement of Fourier transform-infrared (FT-IR) spectra. [Ch][FA] was dissolved in chloroform and dropped onto a potassium bromide tablet. Following volatilization of chloroform, the sample was scanned from 400 to 4000 cm^{-1} . A DSC 204 F1 Phoenix® (Netzsch, Selb, Germany) was used for differential scanning calorimetry (DSC) analysis. About 10 mg of the samples were sealed into an aluminum pan, being heated from -40 to 80 °C at 5 °C/min. An empty aluminum pan was used as a reference. The water content was determined by volumetric Karl Fischer moisture titrator (KEM, Kyoto, Japan).

2.5. Measurement of CAC

ACQ probe (P2) was used to measure the CAC of [Ch][FA]. Briefly, the salt was dissolved in water to obtain a series of solution with concentrations ranging from 0.0001 to 100 mmol/L. P2 was added to the solution (0.17 $\mu\text{mol/L}$), which was incubated at 37 °C overnight under mild shaking. The fluorescent intensities of the solutions were measured by Agilent Cary Eclipse (Santa Clara, CA, USA) (Ex = 708 nm, Em = 732 nm). The fluorescent

intensity vs. concentration profile was drawn. CAC was indicated as the concentration of the transition point (Fig. 2B).

2.6. Molecular dynamics simulation

The molecular structure of oleic acid was downloaded from the open chemistry database of PubChem (PubChem CID: 445639). The choline model was constructed manually. Based on these, two molecular models were constructed. One was a $35 \times 35 \times 35$ Å³ periodic cubic box with 60 [Ch][Ole] pairs. The other was added a layer of water molecules (~ 8477) with a thickness of 6.0 Å on the basis of the first molecular model.

Partial atomic charges of oleate anion and cholinium were calculated by the Gaussian 09 (Gaussian, Inc, Wallingford, CT, USA) package and then the force fields were constructed by the AmberTools 12 (University of California, San Francisco, CA, USA). Molecular dynamics simulation was performed by NAMD 2.14 (University of Illinois at Urbana–Champaign, Champaign, IL, USA) with the prepared general Amber force field¹⁸. Long-range electrostatic interactions were treated with the Particle Mesh Ewald method. A long distance of 15.0 Å was set for the non-bonded cutoff. The time step was set to 2.0 fs for the integration of the movement equations. The temperature was controlled at about 300 K by Langevin dynamics with a damping

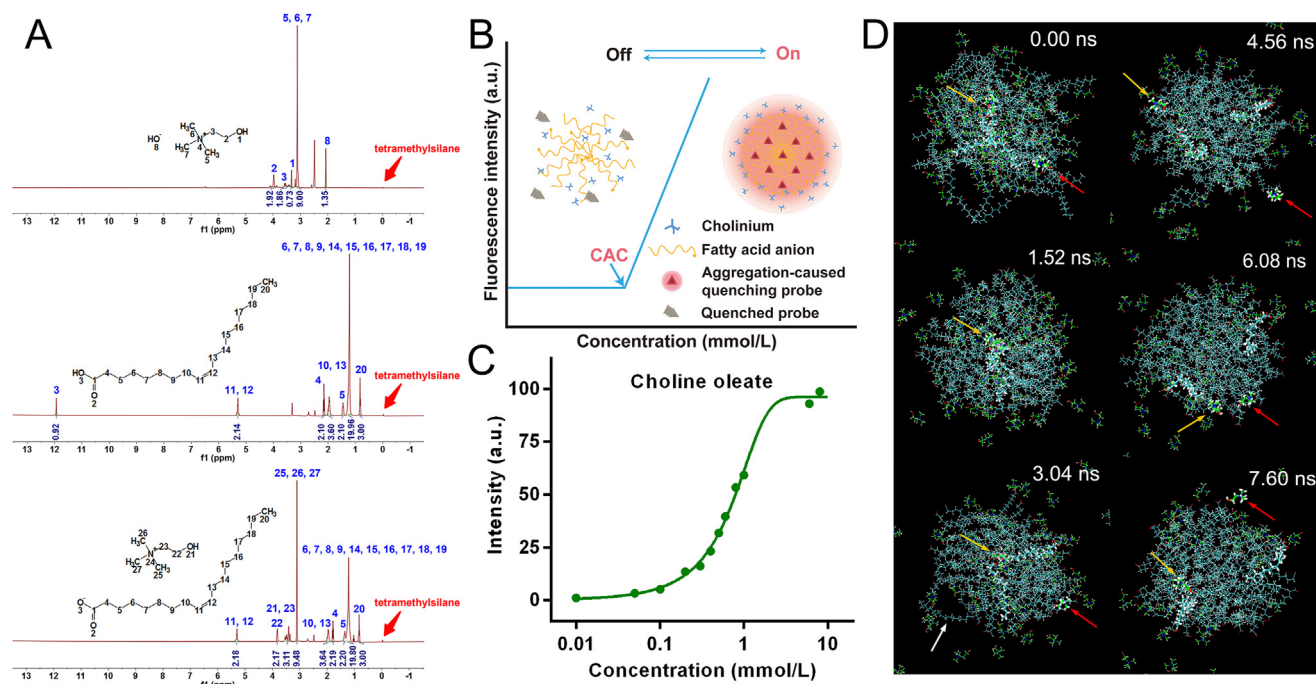


Figure 2 Characterization and molecular dynamics of choline oleate. (A) ¹H NMR spectra of choline, oleic acid, and choline oleate; (B) schematic diagram of critical aggregation concentration measurement *via* the ACQ probes; (C) variation of fluorescent intensity along the concentration of choline oleate; (D) the simulation snaps of co-aggregation of choline oleate in water (water molecules are omitted). The yellow and red arrows indicate two selected choliniums, while the white one indicates the escaped oleate anion.

coefficient of 1 ps^{-1} . The pressure was set to 1 atm. The period and the damping time constant of the Nosé-Hoover Langevin piston was set to 100 fs and 50 fs, respectively. The simulated annealing technology with a step of 100 K was used to prepare the production models.

2.7. Preparation of ICAs

The composition of Taxol® was adopted as a reference to prepare PTX loaded ICAs, which is composed of 6 mg PTX, 527 mg cremophor EL, and 392 mg dehydrated ethanol in each mL of the preparation. Since [Ch][Ole]/ethanol mixture showed stronger solubilizing capacity to PTX than cremophor EL/ethanol mixture ($>171 \text{ mg/g}$ vs. $82.68 \pm 1.51 \text{ mg/g}$), 10-fold amount of PTX was adopted in the preparation of ICAs. In brief, 60 mg PTX was dissolved in 392 mg dehydrated alcohol firstly, which was mixed with 527 mg [Ch][Ole]. The mixture was diluted to a PTX concentration of 1 mg/mL with normal saline to get PTX loaded ICAs. A micellar solution (MCs ($\times 6$)) by diluting Taxol® (30 mg, 5 mL, Bristol Myers Squibb, New York, NY, USA) with normal saline to a PTX concentration of 1 mg/mL was set as a control. Of note is that the amount of cremophor EL in MCs ($\times 6$) is 10-fold that of [Ch][Ole] in ICAs. For comparison, a micellar solution (MCs ($\times 60$)) was prepared using the same procedure in the preparation of ICAs except that [Ch][Ole] was replaced with equal amount of cremophor EL.

The encapsulation efficiency (EE, %) of PTX in ICAs was measured by a centrifugation method. Due to the poor solubility in water, the free PTX precipitates in water and can be separated

from ICAs by centrifugation. ICAs, 1 mL, were centrifuged at 10,000 rpm (TG16-WS high-speed centrifuge, Cence, Changsha, China) for 5 min. The supernatant, 0.8 mL, was diluted to 25 mL with methanol for high performance liquid chromatography (HPLC) measurement of loaded PTX (W_L). In the meantime, 0.8 mL ICAs was diluted to 25 mL with methanol for HPLC measurement of total PTX (W_T). The EE (%) was calculated according to Eq. (1):

$$\text{EE} (\%) = W_L/W_T \times 100 \quad (1)$$

The *in vitro* release of PTX from ICAs was evaluated using a dialysis method¹⁹. ICAs, 1 mL, were sealed in a dialysis bag with a molecular weight cut-off of 8–14 KD, which was immersed in 500 mL phosphate buffer solution (pH7.4) containing 0.5% (*w/v*) Tween 80. Drug release was performed at 37 °C under 100 rpm stirring. At pre-determined intervals, 1 mL release medium was withdrawn and an equal amount of fresh medium was added. Following centrifugation at 12,000 rpm (TG16-WS high-speed centrifuge, Cence, Changsha, China) for 10 min, the supernatant was analyzed by Shimadzu 8040 liquid chromatography couple to tandem mass spectrometry (LC–MS/MS) (Shimadzu Corporation, Kyoto, Japan) for PTX content.

To label the carrier particles, P2/P4 was firstly dissolved in ethanol solution of PTX. The following procedure was the same as that used in the preparation of ICAs. The final concentration of P2/P4 in the formulation was listed in Supporting Information Table S2, which was adjusted to get comparable fluorescent intensities among the preparations.

2.8. Characterization of ICAs

Size and zeta potential of each preparation was measured by Zetasizer Nano (Marven, Worcestershire, UK). Morphology was observed on a Tecnai G2 S-TWIN field emission transmission electron microscope (TEM) (FEI, Hillsboro, OR, USA). The preparation was diluted 10 folds with normal saline. One microliter of the dilution was dropped on copper grids and allowed to air-dry. Observation was performed at 200 kV.

2.9. Absolute bioavailability

The preparations were intraduodenally (i.d.) administered to avoid damage from acidic environment in stomach^{20,21}. In brief, the rats were anesthetized with 0.3 g/kg chloral hydrate *via* intraperitoneal injection; following remove of the abdominal hair, a 1-cm incision was made below xiphoid process; a suture was tied gently ~3 cm distal to the pylorus around the duodenum, preventing the dose from flowing back into the stomach; each preparation at a dose equivalent to 10 mg/kg of PTX was injected 8 cm distal to the pylorus; subsequently, the injection site was sealed by a drop of super glue (Compont Medical Equipment Co., Ltd., Beijing, China), while the suture was removed 3 min later; the abdomen was carefully sutured; at predetermined intervals, 500 μ L blood was collected from the eye socket. The plasma was withdrawn following centrifugation (5000 rpm) for 5 min and kept in -20°C pending analysis.

Meanwhile, P2 labelled ICAs and MCs ($\times 6$) were intravenously (i.v.) injected into sham operated SD rats at a dose equivalent to 5 mg/kg of PTX, respectively. At predetermined intervals, 500 μ L blood was collected from the eye socket. Therein 200 μ L was subjected to measure the fluorescent intensity by IVIS® Spectrum Live Imaging System (PerkinElmer, Branford, USA). The rest blood samples were centrifuged (5000 rpm) for 5 min. The plasma was drawn and kept in -20°C pending analysis.

The plasma, 100 μ L, were mixed with 10 μ L internal standard solution (methanol solution of docetaxel, 1 μ g/mL) by vortex for 1 min. Then, 1 mL equal volume of *tert*-butyl methyl ether and dichloromethane was added into the plasma, followed by vortex for 10 min. The mixture was centrifuged (12,000 rpm) for 10 min, while the organic layer was withdrawn and dried at 40°C . The residual was dissolved in 100 μ L 60% (*v/v*) acetonitrile aqueous solution by vortex for 10 min. Following centrifugation (12,000 rpm) for 10 min, the supernatant, 2 μ L, was injected into the LC-MS/MS (Shimadzu 8040) for PTX content analysis.

A XSelect HSS T3 XP column (2.1 mm \times 100 mm, 2.5 μ m), being maintained at 30°C , was used for separation. The mobile phase consisted of 0.1 mmol/L ammonium formate in deionized water and 0.1 mmol/L ammonium formate in methanol (15:85, *v/v*), being pumped at 0.35 mL/min. An electrospray ionization (ESI) in positive mode was employed. Acquisition was performed in multiple reaction monitoring mode using *m/z* 854.25 \rightarrow 286.05, 808.35 \rightarrow 226.10 ion transitions for paclitaxel and docetaxel, respectively. Data acquisition was controlled and synchronized using Labsolution software (Shimadzu Corporation, Kyoto, Japan). Peak area ratio of PTX to docetaxel (*R*) was used for quantification. Linearity was observed in the concentration (*C*) range of 1–2000 ng/mL with a typical calibration curve: $C = 76.9231R - 3.7615$ ($R^2 = 0.9989$, $n = 6$). Accuracy for the determination ($n = 9$) was $100.01 \pm 1.90\%$. Intra- and inter-day precisions were all below 8%, and the extraction recovery of PTX ($n = 9$) was $83.82 \pm 3.47\%$.

Plasma PTX concentration *vs.* time profiles were drawn. Noncompartmental analysis was performed to obtain the main pharmacokinetic parameters: maximum plasma concentration (C_{\max}), time to reach C_{\max} (T_{\max}), and area under the concentration–time curve (AUC). The absolute bioavailability (*F*) was calculated as shown in Eq. (2):

$$F (\%) = (\text{AUC}_{i.d.}/\text{Dose}_{i.d.})/(\text{AUC}_{i.v.}/\text{Dose}_{i.v.}) \times 100 \quad (2)$$

2.10. Gastrointestinal translocation and *in vivo* distribution

Two milliliters of P2 labelled ICAs, MCs ($\times 6$), and MCs ($\times 60$), was intraduodenally administered to SD rats, respectively. The intraduodenal administration took the same procedures in the bioavailability study. SD rats were sacrificed at predetermined intervals. Gastrointestinal tracts and major organs were immediately imaged by the IVIS® System (PerkinElmer).

2.11. Trans-epithelial transportation

The rats were anesthetized with 0.3 g/kg chloral hydrate *via* intraperitoneal injection. Intestine segment was exposed *via* a midline incision to the abdomen. A closed loop (~ 10 cm) was made in jejunum or ileum segment. P4 labelled ICAs, MCs ($\times 6$), and MCs ($\times 60$) were perfused into the loop, respectively. After 45 min of perfusion, the rats were sacrificed to dissect the jejunum and ileum segment. The segments were then treated with paraformaldehyde solution (4%, *w/v*) and sucrose solution (30%, *w/v*) successively for fixing and dehydration, respectively. Following frozen with OCT compound, the treated segments were cut into 10 μ m slices by Microm CM3050S (Leica, Mannheim, Germany) and stained with DAPI for confocal laser scan microscope (CLSM) (Carl Zeiss Inc., LSM710, Jena, Germany) observation.

2.12. Cellular interaction

The amount of PTX in the preparation was reduced by half for the cellular studies. In brief, 30 mg PTX was dissolved in 392 mg dehydrated ethanol, which was mixed with 527 mg of [Ch][Ole]. The mixture was diluted by DMEM (Dulbecco's modified Eagle medium) medium containing 10% fetal bovine serum to a PTX concentration of 0.03 mg/mL to get ICAs. For comparison, the micelles (MCs) adopted the same formula by replacing [Ch][Ole] with equal amount of cremophor EL. P2 and P4 were added in the preparations for fluorescent labeling. To get comparable fluorescence, concentration of P2 and P4 was 2 and 0.6 μ g/mL in ICAs as well as 1 and 0.3 μ g/mL in MCs, respectively.

Cell culture was performed at 37°C and 5% CO_2 . DMEM medium containing 10% fetal bovine serum was adopted for culture of Caco-2 and HT29-MTX cells. Every two days, the culture medium was replaced, while the cells were passaged. For Raji cells, the culture procedure is similar except that DMEM was substituted by roswell park memorial institute (RPMI) 1640.

Cellular uptake was performed on Caco-2 and Caco-2/HT29-MTX (7:3) co-culture monolayers. The cells were seeded in 96-well plates or glass bottom cell culture dishes in a density of 1×10^5 per cm^2 . The culture lasted 14 d following regular procedures. Then the membranes were treated by P2 labelled ICAs or MCs, and incubated for 4 h. The test samples were discarded at predetermined intervals. Following washing the membranes with phosphate

buffered saline (PBS) three times, the wells were subjected to IVIS[®] imaging system (PerkinElmer) for fluorescence measurement. Meanwhile, PTX that was taken up by the cells was extracted for measurement by HPLC²². 50 μ L water was added into each cell well for 5 freeze–thaw cycles to lyse the cells. The lysed cells were mixed with 100 μ L internal standard solution (methanol solution of docetaxel, 10 μ g/mL). Then, 1 mL methyl tert-butyl ether was added into the tube, which was vortexed for 10 min. The mixture was centrifuged (12,000 rpm) for 10 min. Then the supernatant was collected and dried. The residue was dissolved by 100 μ L acetonitrile–water (45/55, v/v) mixed solution, which was further centrifuged (12,000 rpm) for 10 min. The supernatant was analyzed by HPLC for PTX content. In addition, following incubation for 4 h, the cell membranes were washed by PBS, and stained by DAPI for CLSM (Carl Zeiss Inc.) observation.

Trans-monolayer transport was performed on Caco-2/Raji co-culture monolayers that mimic M cells. Caco-2 cells (1×10^5 per cm^2), were seeded into the apical (AP) side of insert cell culture plate (Jet Bio-Filtration Co., Guangzhou, China, 3 μ m). The culture followed regular procedures until the trans-epithelial electrical resistance (TEER) value remained 300 $\Omega \text{ cm}^2$ or higher for 3 days. Then Raji cells were added to the basolateral (BL) side in a density of 2×10^6 per mL. An obvious decline of the TEER value means the successful infiltration of Raji cells. Then 300 μ L ICAs/MCs and 600 μ L DMEM medium were added into the AP and the BL side, respectively. Following 4 h of cultured, 200 μ L samples were withdrawn from the BL side at predetermined intervals for fluorescence measurements by IVIS[®] (PerkinElmer). Meanwhile, 50 μ L of the sample was transferred to a 1.5 mL tube for extraction of PTX following the same procedure adopted in the cellular uptake.

The extracted PTX was measured by an Agilent 1260 HPLC system (Santa Clara, CA, USA) at 227 nm. A ZORBAX SB-C18 (5 μ m, 4.6 mm \times 250 mm) column was used for separation. The mobile phase consisted of acetonitrile and water in a volume ratio of 45/55 (v/v), which was pumped at 1 mL/min and maintained at 25 $^\circ\text{C}$. Quantification was based on the peak area ratio of PTX to docetaxel. Linearity was observed in the concentration range of 0.30–30 μ g/mL with a typical calibration curve: $C = 4.3559R + 0.0460$, $R^2 = 0.9999$, $n = 8$). Accuracy for the determination ($n = 9$) was $99.78 \pm 2.29\%$. Intra- and inter-day precisions were all below 10%, and the extraction recovery of PTX ($n = 9$) was $78.04 \pm 5.86\%$.

2.13. Statistical analysis

SPSS[®] (version 11.0, IBM, New York, NY, USA) was used to perform the statistical analysis with ANOVA. Values were considered significantly different at $P < 0.05$.

3. Results and discussions

3.1. Synthesis and characterization of [Ch][FA]

[Ch][FA] consisting of choline and different fatty acids were synthesized *via* metathesis reaction. They varied from liquid to semisolid at room temperature when the ions have longer carbon chain length (Supporting Information Fig. S1). This is due to the increased van der Waals or hydrogen bond interactions in ion network²³. Fig. 2A shows the ¹H NMR spectrum of choline, oleic acid, and [Ch][Ole]. The carboxylic proton of oleic acid (peak at

11.93 ppm) was absent in the spectra of [Ch][Ole], while a shift from 2.15 to 1.79 ppm was found for hydrogen adjacent to the carboxyl group. The upfield chemical shift is due to the dissociation of hydrogen on the carboxyl group, which increases the electron density and thus increases the nuclear magnetic shielding of adjacent hydrogen nuclei²⁴. The results confirm the transformation of oleic acids to salts. In addition, ¹H NMR confirms the stoichiometry of 1:1 between the two constituents. Successful syntheses of other [Ch][FA] were also confirmed by ¹H NMR (Supporting Information Fig. S2–S8). Supporting Information Fig. S9 shows the FT-IR spectrum of the [Ch][FA]. It is obvious that the peak of the C=O stretching vibration of the fatty acid (marked with the red dotted line) was shifted from 1711 to 1563 cm^{-1} in the spectrum of [Ch][FA] (marked with the blue dotted line), indicating the conversion of carboxylic acid to carboxylate. Supporting Information Fig. S10 shows the DSC curves. The melting point of [Ch][FA] increased with the chain length of the corresponding fatty acid, being consistent with the appearance. The melting points of [Ch][FA] were all lower than the fatty acid counterparts, which may be due to the asymmetric cholinium. Increase of double bond in the chain of fatty acid further decreased the melting point of both fatty acid and [Ch][FA] (Supporting Information Table S1), *e.g.*, -9 $^\circ\text{C}$ of choline oleate *vs.* 56 $^\circ\text{C}$ of choline stearate and 3–16 $^\circ\text{C}$ of oleic acid *vs.* 67–72 $^\circ\text{C}$ of stearic acid. The melting points of choline linoleate and choline linolenate were even lower than the tested range. In addition, the moisture contents of [Ch][FA] are all below 4% (w/w) (Table S1).

The ACQ probe, P2, was used to measure the CAC of the [Ch][FA]. The underlying mechanism is related to the ACQ properties of the probes (Fig. 2B). Prior to the CAC, the absence of ICAs leads to complete quench of P2. Therefore, the pre-aggregation region presents a plateau with a fluorescent intensity of zero. When the concentration reaches and exceeds the CAC, the probes are encapsulated into the lipophilic cores of the aggregates, leading to the appearance and increase of the fluorescence. The concentration where the fluorescence emerges denotes the CAC of [Ch][FA]. Fig. 2C and Supporting Information Fig. S11 show the variation of fluorescent intensity along the concentration of [Ch][FA]. The CACs of the [Ch][FA] were summarized in Table S1. The one involved longer chain length fatty acids shows lower CAC due to the increased lipophilicity of the anion. No fluorescence was observed from the aqueous solution of [Ch][FA] consisting of fatty acids with chain length less than 10 carbons, indicating absence of ICAs. The reason is due to the higher aqueous solubility of the short-chain and middle-chain fatty acids than the long-chain ones. The anions can be fully dissociated from the choline cations in water. On the contrary, fatty acids that have more than 10 carbons are insoluble in water and extremely hydrophobic. Unsaturated bond also decreases the CAC of [Ch][FA], *e.g.*, 0.19 ± 0.01 mmol/L of choline oleate *vs.* 0.37 ± 0.02 mmol/L of choline stearate. These results are similar in the critical micelle concentration (CMC) of surfactants containing fatty acids such as Tween. Increase in the number of unsaturated bonds further decreases the CAC of [Ch][FA], *e.g.*, 2.02 ± 0.01 mmol/L of choline linoleate and 0.55 ± 0.001 mmol/L of choline linolenate. The mechanisms are still unclear. Nonetheless, the CAC of [Ch][Ole] is far below the CMC of commonly used surfactants, implying strong solubilizing capability. Since both oleic acid and choline are listed in GRAS (generally recognized as safe) of FDA, [Ch][Ole] was adopted for the following investigations.

3.2. Molecular dynamics simulation

Fig. 2D shows the simulation snapshots of the co-aggregation of [Ch][Ole] in water. The dynamic process can be found in Supporting Information Video. For clarity, the carbon chain of oleate anion is marked with darkcyan, while that of cholinium is marked with green. The skeletons of two oleate anions and two choliniums are shown as sticks. Both the two oleate anions are in the center, while the choliniums are in the center (indicated by yellow arrow) and the surface (indicated by red arrow) of the molecular mixture, respectively. Initially (0.00 ns), oleate anions and choliniums were arranged randomly. With the introduction of water, the oleate anions were compacted to form aggregate, while choliniums diffused toward the surrounding water environment. At 1.52 ns, all oleate anions on the surface of the aggregate have taken directional arrangement, *i.e.*, the carboxyl anions facing the external aqueous environment and the hydrophobic carbon chains facing inward. The internal oleate anions become more compacted than the initial extension state. Choliniums in the aqueous environment are in dynamic interaction with the carboxyl anions. The red arrow indicated cholinium diffused out of the visual field, which returned to bind the carboxyl anions on the surface of the aggregate at 3.04 ns. The internal cholinium stayed put in the meantime, which didn't diffuse to the surface of the aggregate until 4.56 ns. Then both two choliniums roll over the surface of the aggregate, being in dynamic co-aggregation with the oleate anions. Interestingly, the orientation of the internal oleate anion transitioned continuously until the carboxyl anions faced the outward aqueous environment. At 3.04 ns, one of the internal oleate anions had stretched horizontally with the carboxyl anions outward and the carbon chain inward. In the meantime, the other one was in vertical orientation. The carboxyl anion was still buried inside the aggregate. The carboxyl head rotated counterclockwise at 4.56 ns and reached the surface of the aggregate at 6.08 ns. Then the carbon chain tail waged inward. Finally, almost all carboxyl anions were on the outside of the aggregate at 7.60 ns, while choliniums were in dynamic co-aggregation with the carboxyl anions. Only one oleate anion migrated to the aqueous environment (indicated with white arrow at 3.04 ns) throughout the process. It is reported that the sodium salts were completely dissociated from the carboxylates in aqueous solutions of fatty acid salts²⁵, consequently, leading to partial hydrolysis of the carboxylates and precipitation of the formed fatty acid. On the contrary, substitution of alkaline salts with organic ammoniums (*e.g.*, tetrabutylammonium and tetraalkylammonium) decreases CMC of anionic surfactants because they have stronger interaction with carboxylates. We therefore infer that the bulky quaternary ammonium headgroup of choline are crucial for the structural integrity, although the co-aggregation is in dynamic. Theoretically, ICAs may be constructed by other combination of lipophilic ions and hydrophilic counter-ions. The molecular mechanisms that govern the formation of ICAs are yet to be explored.

Supplementary video related to this article can be found at <https://doi.org/10.1016/j.apsb.2022.04.011>

3.3. Preparation and characterization of ICAs

TEM shows the morphology of ICAs, which are spherical and in the range of 10–50 nm (Fig. 3A). A dual size distribution was

observed from the dynamic light scattering (DLS) measurement. The primary distribution ranged from several nanometers to 50 nm with a mean size of 12.53 ± 0.164 nm, while the secondary one was from 1000 to 6000 nm (Fig. 3B). The large size may be due to the agglomeration of a small portion of ICAs. The polymer dispersity index (PDI) of ICAs is 0.208 ± 0.012 , implying a homogenous size distribution. MCs ($\times 60$) and MCs ($\times 6$) show similar morphology and size distribution with a mean size around 14 nm (Fig. 3A and B). The agglomeration of the micelles is obvious, while the morphology is not spherical. The reason is ascribed to the increased concentration of cremophor EL in the drying of the copper grids, which increases interparticle interactions and leads to hexagonal packing²⁶. Nonetheless, the DLS measurement generally supports the results of the TEM for all preparations. The size and the morphology of ICAs were similar to micelles. Moreover, the zeta potential of ICAs is -25.6 ± 4.43 mV, being due to the dissociation of a part of choliniums from the surface of the ICAs. MCs ($\times 60$) and MCs ($\times 6$) are electrically neutral (Table S2).

A centrifugation method was adopted to measure the EE (%) of PTX in ICAs. To examine the feasibility of the method, P2 labeled ICAs were centrifuged at 10,000 rpm for 5 min. The IVIS[®] (PerkinElmer) imaging before and after centrifugation indicated that the centrifugation condition did not cause precipitation of ICAs (Supporting Information Fig. S12 A). Meanwhile, 1 mL PTX suspension (1 mg/mL, *w/v*) was centrifuged at 10,000 rpm for 5 min. All PTX was precipitated in the bottom of the tube and no PTX could be detected in the supernatant. Based on the method, the EE (%) of PTX in ICAs was $98.2 \pm 1.5\%$. Fig. S12 B shows the release of PTX from ICAs, being in a sustained release manner. Only 30% was released in 48 h. This is ascribed to the good solubilizing capability of ICAs.

3.4. Oral bioavailability

Fig. 3C and D shows the plasma concentration–time curves following administration of the preparation *via* intraduodenal or intravenous route, respectively. Table 1 summarizes the main pharmacokinetic parameters. The profiles following *i.d.* administration are similar to the reported results of oral Taxol[®], *i.e.*, a fast absorption and a slow elimination^{27–29}. MCs ($\times 60$) and MCs ($\times 6$) reached C_{\max} at 1 h post administration, which is within the range of t_{\max} of orally administered Taxol[®] (0.3–2 h)^{27–29}. The absorption of ICAs was a slight faster than that of MCs ($\times 60$) and MCs ($\times 6$), which reached C_{\max} at 0.5 h post administration. The plasma concentrations gradually decreased to 0.018 $\mu\text{g/mL}$ from T_{\max} to 2 h post administration of ICAs, which fluctuated around this level till 48 h. Similarly, a platform concentration around 0.02 $\mu\text{g/mL}$ presented between 4 and 8 h in the profile of MCs ($\times 6$), which decreased to 0.014 $\mu\text{g/mL}$ and gradually to 0.007 $\mu\text{g/mL}$ at 48 h. On the contrary, the plasma concentration of PTX quickly decreased to 0.004 $\mu\text{g/mL}$ at 8 h post administration of MCs ($\times 60$). The AUC of ICAs is comparable to that of MCs ($\times 6$) but 2.48 folds that of MCs ($\times 60$). It is noteworthy that the amount of carrier materials of ICAs is equal to that of MCs ($\times 60$), but only one-tenth that of the MCs ($\times 6$). The results imply the better solubilizing and permeation enhancing ability of ICAs than cremophor EL micelles.

The pharmacokinetics of ICAs and MCs ($\times 6$) *via* intravenous administration were obtained to quantify the absolute oral bioavailability. The plasma concentration *vs.* time plots are shown in Fig. 3D, which decreased quickly post *i.v.* administration.

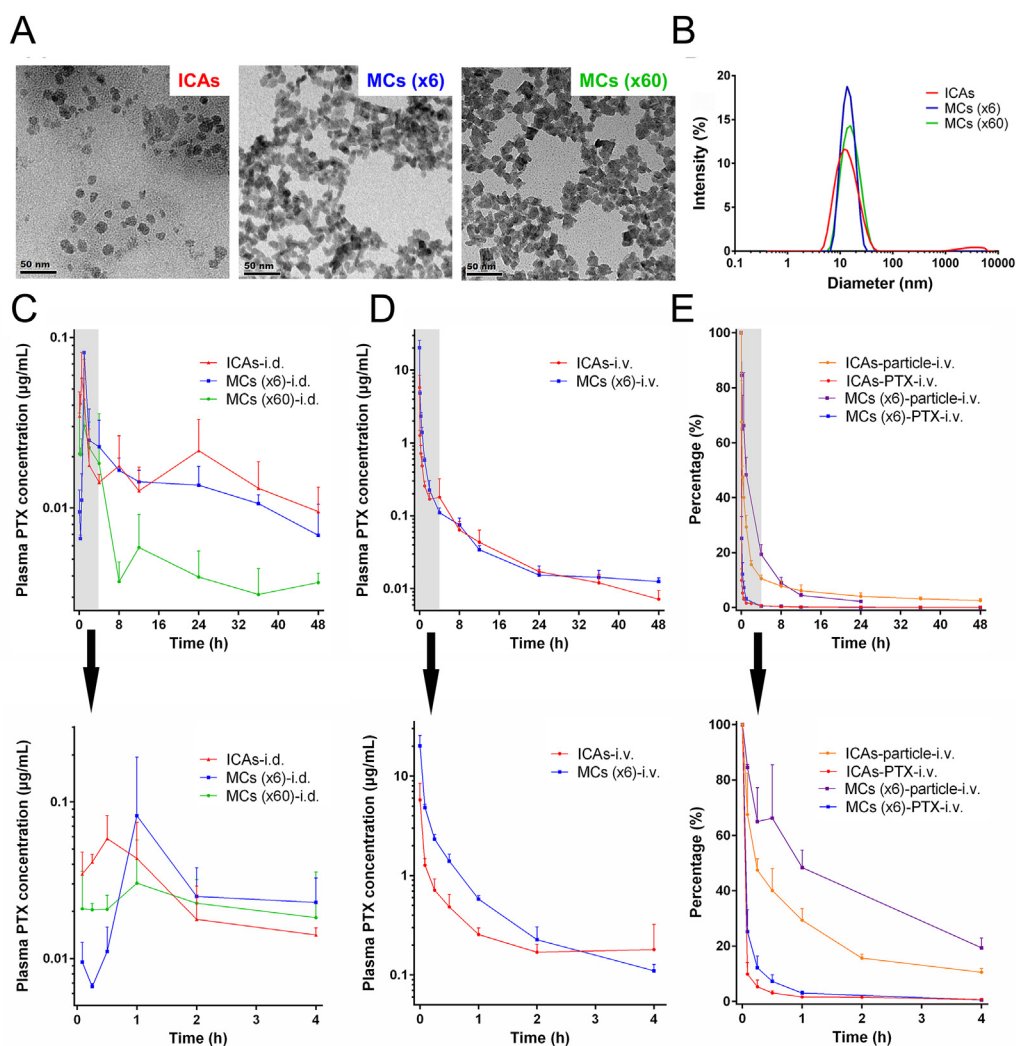


Figure 3 Characterization and pharmacokinetics of ICAs, MCs ($\times 6$), and MCs ($\times 60$). (A) Morphology and (B) size distribution of ICAs, MCs ($\times 6$), and MCs ($\times 60$); plasma concentration vs. time profiles of paclitaxel *via* (C) intraduodenal administration of ICAs, MCs ($\times 6$), and MCs ($\times 60$) as well as (D) intravenous injection of ICAs and MCs ($\times 6$) ($n = 3$); (E) comparison between the pharmacokinetics of paclitaxel and carrier particles following intravenous administration of ICAs and MCs ($\times 6$). The values were indicated as the normalized plasma concentration of paclitaxel and fluorescent intensity that was set with the value of the first sampling as 100% ($n = 3$).

Although the plasma PTX levels from 8 to 48 h were similar for both two preparations, ICAs showed faster elimination than MCs ($\times 6$) in the initial 4 h. Since PTX concentrations in the initial stage were significantly higher than that in the latter one, the AUC of the intravenously injected ICAs is nearly half that of the MCs ($\times 6$). The reduced elimination of MCs ($\times 6$) may be due to the long-circulating ability. Cremophor EL is polyoxyethylated castor oil, being able to form micelles with polyoxyethylene as the shell²⁶. Polyoxyethylene is the gold stand of decorating material to achieve long-circulating as it reduces plasma protein adsorption (opsonisation) due to the hydrophilicity^{30,31}. Based on the AUC of corresponding preparation *via* intravenous route, the absolute oral bioavailability of ICAs, MCs ($\times 6$), and MCs ($\times 60$) amounts to 12.46%, 8.66%, and 2.99%, respectively. Although ICAs showed similar AUC to MCs ($\times 6$) following oral administration, the absolute oral bioavailability of ICAs is even higher than that of MCs ($\times 6$).

Blood pharmacokinetic profiles of the carrier particles (Fig. 3E) validate the longer circulation of MCs ($\times 6$) than ICAs. A quantitative relationship between the fluorescence intensity of the ACQ probes and the relative quantity or mass of the intact nanocarriers has been validated in previous studies^{32–36}. The pharmacokinetic profile of the carrier particles was indicated with the normalized fluorescence that was set with the value of the first sampling as 100%. Both ICAs and MCs ($\times 6$) eliminated fast in blood with typical “L”-type biphasic kinetics. For ICAs, only 50 and 20% fluorescence level remained at 15 min and 4 h, respectively. However, the elimination of MCs ($\times 6$) was slower than that of ICAs during the first 4 h, as indicated by the significantly higher blood fluorescence levels in the same time points. The results validate the prolonged circulation of MCs ($\times 6$) in blood. In addition, the plasma PTX levels were normalized with the same way to compare the pharmacokinetics between the cargos and the carrier particles. A huge gap presents in the level between PTX

and the carrier particles, irrespective of the carrier type. The results are similar to our previous findings in PTX loaded polymeric nanoparticles, indicating fast leakage of PTX from nanoparticles³³. It is noteworthy that the leakage is not due to the dissociation of the carrier particles, which can be monitored by the ACQ probe. We assume that the leakage may be due to extraction of blood proteins as the plasma protein binding of PTX is greater than 90%³⁷.

3.5. Intestinal translocation and *in vivo* distribution

P2 labeled preparations were administered to study the intestinal translocation and *in vivo* distribution of the carrier particles (Fig. 4). Fig. 4A shows the intestinal translocation of the carriers. The fluorescent signal can be seen as long as 12 h for ICAs, indicating a long intestinal retention. The overall fluorescent level from ICAs was stronger than that from MCs ($\times 60$) and MCs ($\times 6$). An obvious migration from duodenum to ileum was seen for ICAs within 12 h post administration. However, only faint fluorescence remained in the intestinal tract after 4 h for MCs ($\times 60$) and MCs ($\times 6$). The difference implies the better stability of ICAs in the intestinal tract than cremophor EL micelles. Lipolysis of castor oil that composes the lipophilic section of cremophor EL may account for the break of the micelles in the intestinal tract²⁶. These results are in accordance with the pharmacokinetics. The long retention of ICAs with high concentration facilitates the continuous absorption of PTX in the intestinal tract, maintaining a fluctuation of PTX concentration in the plasma till 48 h post administration. The significant decrease of fluorescent intensity after 4 h indicates the break of the micelles and the precipitation of PTX. Accordingly, a significant decrease of plasma concentration of PTX was observed from 4 to 8 h post administration for MCs ($\times 60$) and MCs ($\times 6$). Based on these results, it is inferred that the enhanced oral bioavailability from ICAs may be partly due to the better stability of ICAs in intestinal tract and thus the stronger solubilizing capability *in vivo* than the micelles.

Fig. 4B shows the imaging of dissected major organs. Fluorescence appeared in the liver of rats treated with ICAs, implying absorption of intact ICAs across the intestinal epithelia and distribute in the body. Similarly, intact nanoparticles (nanocrystals^{35,36}, polymeric nanoparticles³⁸, nanoemulsions^{34,39}, and micelles¹⁰) that survive the harsh gastrointestinal environment are able to transepithelially transport and accumulate in major organs. On the contrary, no fluorescence was observed in the organs of rats treated by MCs ($\times 60$) and MCs ($\times 6$). The difference between ICAs and the micelles may be related to their stability in the intestinal tract. As shown in Fig. 4A, the fluorescence of MCs

($\times 60$) and MCs ($\times 6$) almost disappeared at 8 h post administration, while the overall intensity of the micelles in the intestinal tract was lower than that of ICAs. Even if the intact micelles can be transmembrane transported and distributed in the body, the fluorescence is negligible. Taking together the results in Fig. 4A and B, the enhanced oral bioavailability from ICAs is due to the excellent solubilizing ability in the intestinal tract and the transmembrane absorption of the intact ICAs.

3.6. Trans-epithelial transportation

Confocal imaging confirms the transmembrane translocation of intact ICAs (Fig. 5). P4 signals, representing the intact carrier particles, were observed on the BL side of the intestinal membranes. Consequently, the transmembrane transported ICAs may enter the blood circulation *via* lymph and distribute to major organs. However, we didn't detect fluorescence in blood following intraduodenal administration of ICAs, while the fluorescence signal of ICAs only appeared in liver (Fig. 4B). The reason may be due to the limited amount of the transmembrane transported ICAs. Our previous studies show that the systemic exposure of orally administered nanocarriers is less than 5% of the dose^{10,35,36,38,39}. The blood fluorescence of ingested carriers was thus negligible. However, blood-circulating particles are doomed to be opsonized and captured by macrophages residing in RES (reticular endothelial system) organs. Due to the rapid blood flow in liver and the large opening of the capillaries, majority of the blood circulating ICAs accumulated in liver. Similar results were found in oral delivered nanocrystals^{35,36}, polymeric nanoparticles³⁸, micelles¹⁰, and nanoemulsions³⁹. Nonetheless, signal intensities of the samples treated by ICAs are much stronger and locate deeper than MCs ($\times 6$). Of note is the difference between *in situ* perfusion and intraduodenal gavage. The closed loop reduces the lipolysis of cremophor EL; even so, only faint fluorescence signal of MCs ($\times 6$) was observed in the BL side of the intestinal membranes. While for MCs ($\times 60$), the fluorescence in the BL side is negligible. The results support the better transmembrane capacity of ICAs than cremophor EL micelles.

3.7. Cellular uptake

Cellular uptake of PTX and intact ICAs/MCs was examined using Caco-2 cell culture (Fig. 6). In Caco-2 cell model, the uptake of PTX increased with extended incubation time. The maximum uptake of PTX reached $9.56 \pm 0.61\%$ and $3.35 \pm 0.91\%$ following 4 h incubation when being delivered by ICAs and MCs, respectively. Conversely, uptake of PTX in Caco-2/HT29-MTX encountered a bottleneck, which fluctuated around 2 and 1% for

Table 1 The main pharmacokinetic parameters of the preparations following intraduodenal and intravenous administration^a.

Parameter	ICAs		MCs ($\times 6$)		MCs ($\times 60$)	
	i.v.	i.d.	i.v.	i.d.	i.d.	i.d.
C_{\max} ($\mu\text{g/mL}$)	5.76 ± 2.19	0.07 ± 0.02	20.20 ± 4.45		0.04 ± 0.02	0.10 ± 0.08
T_{\max} (h)	—	0.5	—		1.0	1.0
AUC ($\mu\text{g}\cdot\text{h/mL}$)	2.89 ± 0.72	0.72 ± 0.16	4.85 ± 0.19		0.29 ± 0.08	0.84 ± 0.27
F (%)	—	12.46	—		2.99	8.66

ICAs, ionic co-aggregates; MCs, micelles; i.v., intravenous injection; i.d., intraduodenally; C_{\max} , maximum plasma concentration; T_{\max} , time to reach C_{\max} ; AUC, area under the concentration–time curve; F , absolute bioavailability; —, not applicable.

^aData are presented as mean \pm SD ($n = 3$).

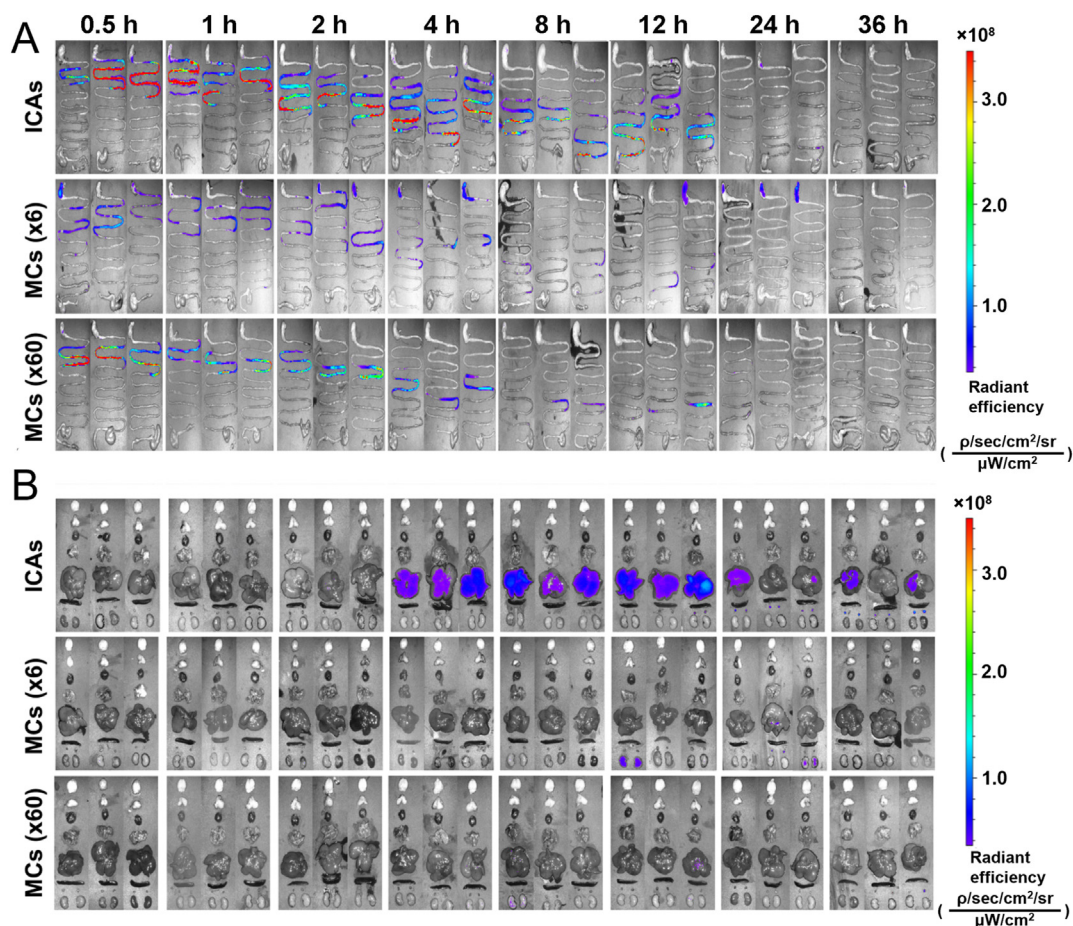


Figure 4 Intestinal translocation and *in vivo* distribution of carrier particles that are monitored by the fluorescence of P2. (A) *Ex vivo* live images of the intestinal tract of rats treated with ICAs, MCs ($\times 6$), and MCs ($\times 60$); (B) *ex vivo* live images of organs (from top to bottom: brain, thyroid gland, heart, lung, liver, spleen, adrenal gland, and kidney) of rats treated with ICAs, MCs ($\times 6$), and MCs ($\times 60$).

ICAs and MCs, respectively. The mucus layer that is secreted by HT29-MTX cells accounts for the difference^{35,36}. ICAs significantly enhanced the cellular uptake of PTX compared to MCs in both cell models (Fig. 6A), supporting the enhanced oral bioavailability. The enhanced permeability from unsaturated fatty acids-bearing micellar systems has been well acknowledged^{40–45}. Concerning the effects of oleic acid, two underlying mechanisms are involved^{46,47}: oleic acid enhances the paracellular permeability by stimulating calmodulin and calmodulin-dependent protein kinase-mediated Ca^{2+} channels to rise intracellular calcium levels; oleic acid has permeation enhancing and P-gP inhibition activity.

Live imaging confirms the internalization of both ICAs and MCs by the presence of the fluorescence of the ACQ probes (Fig. 6B). Like the uptake of PTX, the fluorescence intensity increased gradually with the incubation time. Judged by the fluorescence intensity, more ICAs were internalized than MCs in the same cell model, being consistent with the cellular uptake of PTX. The uptake rate of the intact carriers was calculated *via* the fluorescence measured on cells and the initial value of the formulations (Fig. 6C). Fewer carriers were internalized by the cell than the uptake of PTX. The result implies that some PTX molecules are released from the carriers and ingested by Caco-2 cells. Although PTX is a substrate of P-gP, the P-gP efflux can be inhibited by oleic acid and cremophor EL^{46,47}. Moreover, the

internalization of MCs is similar in both cell models during the experimental period except at the initial incubation of 0.5 h, where the uptake in Caco-2 is higher than that in Caco-2/HT29-MTX. The discrepancy is due to the mucus barrier, where the dense network of mucin fibers hinders the uptake of both therapeutic drugs and carriers. PEGylation is an effective approach to promote mucus-penetration as the slippery surface reduces the interaction between the particles and mucus^{48–50}. The PEG containing cremophor EL thus facilitates mucus-penetration of nano-carriers⁵¹. Consequently, the uptake of MCs in Caco-2/HT29-MTX was slightly retarded by the mucus layer at the initial incubation period but reached the same level to that in Caco-2 afterwards. More ICAs were taken up by the two cell models than MCs. One reason is due to the negative effect of PEGylation, which may hinder the uptake of nanoparticles by reducing their interactions with epithelia⁹. The other is related to the lipid digestion and absorption in gastrointestinal tract⁵². The dietary lipids are digested into fatty acids and monoglycerides in gastrointestinal tract, which form colloidal structures (*e.g.*, vesicles and micelles) to facilitate absorption⁵². ICAs resemble the intermediate colloids of lipid digestion and hence a high uptake from Caco-2 cells. However, it is weird that more ICAs were taken up by Caco-2/HT29-MTX than Caco-2. We infer that some ICAs were trapped in the network of mucin fibers, which is negatively charged. Albeit being

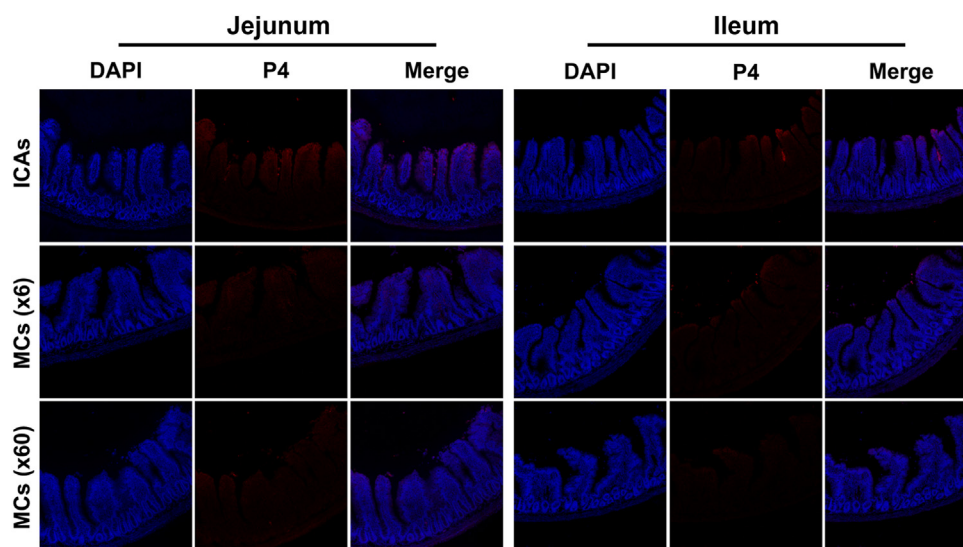


Figure 5 CLSM images of cryostat sections of jejunum and ileum after *in situ* perfusion with ICAs, MCs ($\times 60$), and MCs ($\times 6$) to rats.

negative in zeta potential, the surface of ICAs is covered by positively charged choliniums, being a bridge to trap ICAs in mucus. Therefore, bioadsorption should be excluded to further confirm the internalization of intact carriers.

The confocal images confirm the cellular uptake of intact ICAs and MCs, as the fluorescence signal of intact carriers is coplanar with cell nuclei (Fig. 6D and E). The individual formulation showed similar fluorescent intensity in the two cell models. But stronger fluorescence signal was observed in cells treated by ICAs than that by MCs (indicated by white arrows). The confocal images are generally in agreement with the cellular uptake, supporting the excellent permeability of ICAs. Moreover, it is interesting to find that the mucus layer has minor effects on the internalization of

ICAs, although a portion of the carriers may be trapped in the layer. The exact mechanisms concerning the mucus-penetration and cellular uptake of ICAs need to be further explored.

3.8. Transcellular transport

Transcellular transport of PTX and intact ICAs/MCs was examined in Caco-2/Raji co-culture monolayers (Fig. 7). Like the cellular uptake, transcellular transport of PTX increased with the incubation time (Fig. 7A). The maximum transport of PTX reached 10 and 5% for ICAs and MCs, respectively. Although the values are close to the maximum uptake of PTX in Caco-2 cells, it doesn't mean that the ingested PTX can completely cross the cell

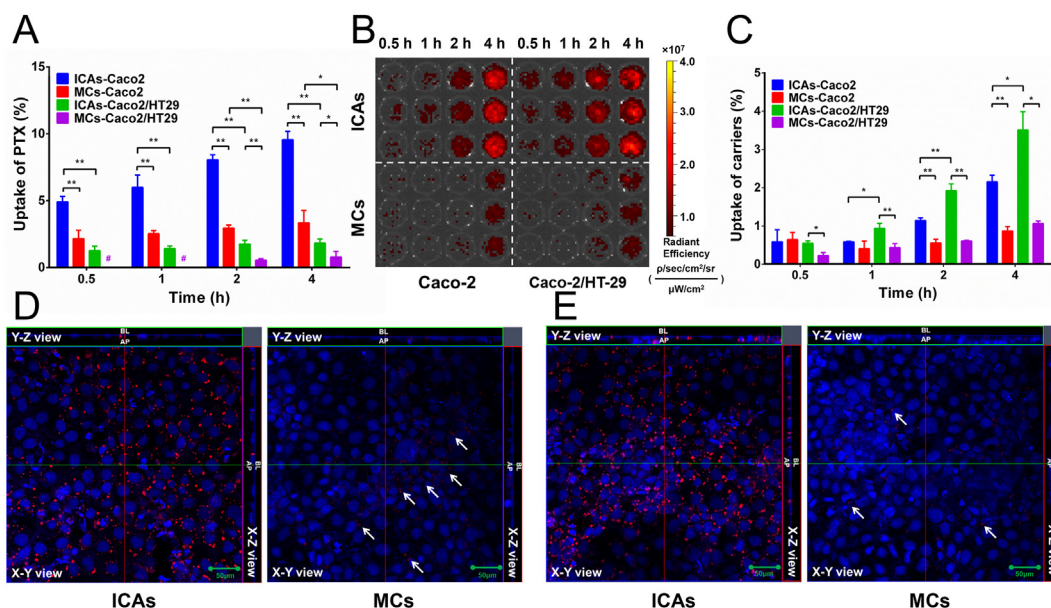


Figure 6 Cellular uptake of ICAs and MCs. (A) Cellular uptake of PTX by Caco-2 and Caco-2/HT29-MTX; (B) live images and (C) quantification of cellular uptake of intact ICAs and MCs by Caco-2 and Caco-2/HT29-MTX; CLSM images visualize the internalization of intact ICAs and MCs in (D) Caco-2 and (E) Caco-2/HT29-MTX monolayers (white arrows indicate the faint fluorescent signals of MCs). (Data are presented as mean \pm SD, $n = 3$; * $P < 0.05$; ** $P < 0.01$ vs. indicated; # indicates lower than detection limit).

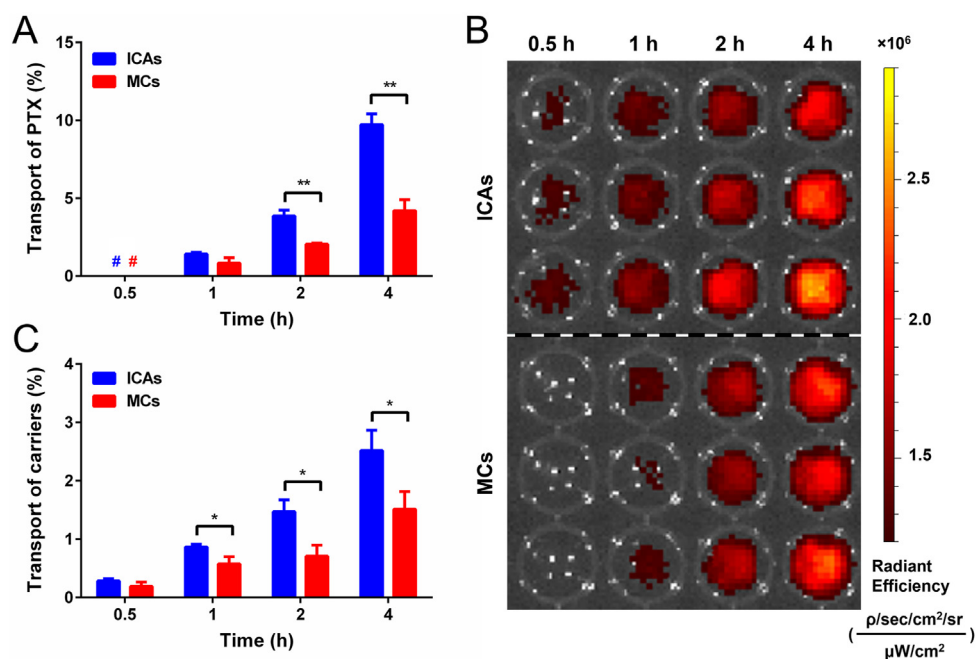


Figure 7 Transcellular transport of ICAs and MCs. (A) Transcellular transport of PTX by Caco-2/Raji; (B) live images and (C) quantification of transport of intact ICAs and MCs by Caco-2/Raji. Data are presented as mean \pm SD, $n = 3$; * $P < 0.05$; ** $P < 0.01$ vs. indicated; # indicates lower than detection limit.

monolayer. Conversely, the transport of PTX in the first 2 h of incubation was far less than the uptake of PTX, while PTX content in the receiving media was lower than the limit of quantitation at 0.5 h of incubation. The high transport may be due to the co-cultured Raji cells, as negligible PTX was transported in the Caco-2 monolayer. Nonetheless, the transport of PTX from ICAs was significantly higher than that from MCs, indicating stronger transport capacity of ICAs.

Live imaging also confirms the transcellular transport of intact ICAs and MCs by the presence of P2 signals in the receiving media (Fig. 7B). Of note is that Caco-2/Raji co-culture monolayers mimic M cells, which are strong in transcytosis transport of particulate materials. No ICAs or MCs could be transported across the Caco-2 monolayer. The fluorescence intensity increased gradually with the incubation time. The transcellular transport percentage of the intact carriers is shown in Fig. 7C. The transport of ICAs was significantly higher than that of MCs except at 0.5 h of incubation. The maximum transport reached 2.5 and 1.5% for ICAs and MCs, respectively. Like the cellular uptake, less carriers were transported cross the cellular monolayer than PTX. The reason is due to the degradation of nanocarriers in the intracellular milieu⁵³.

4. Conclusions

A series of surface active [Ch][FA] have been synthesized and characterized. The CACs of the [Ch][FA] decrease with the increase of the chain length and the number of unsaturated bonds of the fatty acids. Molecular simulation reveals the dynamic co-aggregation of cholinium and oleate anions in water. [Ch][Ole]-based ICAs show similar particle size distribution and morphology to cremophor EL-based micelles. However, ICAs enhance oral

bioavailability of PTX than cremophor EL micelles. The ACQ fluorescence can be utilized to probe the integrity of intact ICAs and micelles. Live imaging of *ex vivo* intestinal tracts of rats shows better stability of ICAs than MCs in intestinal tract. Imaging results reveal that intact ICAs can permeate across intestinal epithelia and accumulate in liver. Caco-2 cell models further support the transepithelial transport of ICAs and the enhanced absorption of PTX. Overall, the enhanced absorption associating with ICAs is due to good stability in intestinal tract to solubilize PTX and the strong transmembrane transport capacity.

Acknowledgments

This work was supported by the National Natural Science Foundation of China (Nos. 82030107, 81973247, 81872815, 81872826, and 81690263) and Science and Technology Commission of Shanghai Municipality (Nos. 19XD1400300, 19430741400, and 19410761200, China).

Author contributions

Xianzi Zheng and Weizi Huang synthesized the materials and the preparation. Zhezheng Fang performed characterization and the cellular experiments. Xianzi Zheng performed the animal studies. Xiaochun Dong and Weili Zhao synthesized the ACQ probes. Jianping Qi guided the cellular experiments. Wei Wu revised the manuscript. Yi Lu designed the study and wrote the manuscript. All of the authors have read and approved the final manuscript.

Conflicts of interest

The authors declare no conflict of interest.

Appendix A. Supporting information

Supporting data to this article can be found online at <https://doi.org/10.1016/j.apsb.2022.04.011>.

References

- Huang WZ, Wu XY, Qi JP, Zhu QG, Wu W, Lu Y, et al. Ionic liquids: green and tailor-made solvents in drug delivery. *Drug Discov Today* 2020;**25**:901–8.
- Vithani K, Jannin V, Pouton CW, Boyd BJ. Colloidal aspects of dispersion and digestion of self-dispersing lipid-based formulations for poorly water-soluble drugs. *Adv Drug Deliv Rev* 2019;**142**:16–34.
- Malamatari M, Taylor KMG, Malamataris S, Douroumis D, Kachrimanis K. Pharmaceutical nanocrystals: production by wet milling and applications. *Drug Discov Today* 2018;**23**:534–47.
- Davis M, Walker G. Recent strategies in spray drying for the enhanced bioavailability of poorly water-soluble drugs. *J Control Release* 2018;**269**:110–27.
- Strickley RG. Solubilizing excipients in oral and injectable formulations. *Pharm Res* 2004;**21**:201–30.
- Al-Ali AAA, Nielsen RB, Steffansen B, Holm R, Nielsen CU. Nonionic surfactants modulate the transport activity of ATP-binding cassette (ABC) transporters and solute carriers (SLC): relevance to oral drug absorption. *Int J Pharm* 2019;**566**:410–33.
- Maher S, Mrsny RJ, Brayden DJ. Intestinal permeation enhancers for oral peptide delivery. *Adv Drug Deliv Rev* 2016;**106**:277–319.
- Zoya I, He HS, Wang LT, Qi JP, Lu Y, Wu W. The intragastric fate of paclitaxel-loaded micelles: implications on oral drug delivery. *Chin Chem Lett* 2021;**32**:1545–9.
- Ahmad E, Lv YJ, Zhu QG, Qi JP, Dong XC, Zhao WL, et al. TAT modification facilitates nose-to-brain transport of intact mPEG-PDLLA micelles: evidence from aggregation-caused quenching probes. *Appl Mater Today* 2020;**19**:100556.
- He HS, Wang LT, Ma YH, Yang YQ, Lv YJ, Zhang ZC, et al. The biological fate of orally administered mPEG-PDLLA polymeric micelles. *J Control Release* 2020;**327**:725–36.
- Castells MC, Phillips EJ. Maintaining safety with SARS-CoV-2 vaccines. *N Engl J Med* 2020;**384**:643–9.
- de Vrieze J. Pfizer's vaccine raises allergy concerns. *Science* 2021;**371**:10–1.
- Glover RE, Urquhart R, Lukawska J, Blumenthal KG. Vaccinating against COVID-19 in people who report allergies. *BMJ* 2021;**372**:n120.
- Bruusgaard-Mouritsen MA, Johansen JD, Garvey LH. Clinical manifestations and impact on daily life of allergy to polyethylene glycol (PEG) in ten patients. *Clin Exp Allergy* 2021;**51**:463–70.
- Stone CA, Liu YW, Relling MV, Krantz MS, Pratt AL, Abreo A, et al. Immediate hypersensitivity to polyethylene glycols and polysorbates: more common than we have recognized. *J Allergy Clin Immunol Pract* 2019;**7**:1533–40.
- Qi JP, Hu XW, Dong XC, Lu Y, Lu HP, Zhao WL, et al. Towards more accurate bioimaging of drug nanocarriers: turning aggregation-caused quenching into a useful tool. *Adv Drug Deliv Rev* 2019;**143**:206–25.
- Lu Y, Lv YJ, Li TL. Hybrid drug nanocrystals. *Adv Drug Deliv Rev* 2019;**143**:115–33.
- Phillips JC, Hardy DJ, Maia JDC, Stone JE, Ribeiro JV, Bernardi RC, et al. Scalable molecular dynamics on CPU and GPU architectures with NAMD. *J Chem Phys* 2020;**153**:044130.
- Guo P, Song SS, Li Z, Tian Y, Zheng JT, Yang XG, et al. *In vitro* and *in vivo* evaluation of APRPG-modified angiogenic vessel targeting micelles for anticancer therapy. *Int J Pharm* 2015;**486**:356–66.
- Nomura D, Saito M, Takahashi Y, Takahashi Y, Takakura Y, Nishikawa M. Development of orally-deliverable DNA hydrogel by microemulsification and chitosan coating. *Int J Pharm* 2018;**547**:556–62.
- Shiels RG, Hewage W, Vidimce J, Pearson AG, Grant G, Wagner KH, et al. Pharmacokinetics of bilirubin-10-sulfonate and biliverdin in the rat. *Eur J Pharmaceut Sci* 2021;**159**:105684.
- Morelli L, Gimondi S, Sevieri M, Salvioni L, Guizzetti M, Colzani B, et al. Monitoring the fate of orally administered PLGA nanoformulation for local delivery of therapeutic drugs. *Pharmaceutics* 2019;**11**:658.
- Huddleston JG, Visser AE, Reichert WM, Willauer HD, Broker GA, Rogers RD. Characterization and comparison of hydrophilic and hydrophobic room temperature ionic liquids incorporating the imidazolium cation. *Green Chem* 2001;**3**:156–64.
- Md Moshikur R, Chowdhury MR, Fujisawa H, Wakabayashi R, Moniruzzaman M, Goto M. Design and characterization of fatty acid-based amino acid ester as a new “green” hydrophobic ionic liquid for drug delivery. *ACS Sustain Chem Eng* 2020;**8**:13660–71.
- Campbell AN, Lakshminarayanan GR. Conductances and surface tensions of aqueous solutions of sodium decanoate, sodium laurate, and sodium myristate, at 25° and 35°. *Can J Chem* 1965;**43**:1729–37.
- Suys EJA, Warren DB, Pham AC, Nowell CJ, Clulow AJ, Benameur H, et al. A nonionic polyethylene oxide (PEO) surfactant model: experimental and molecular dynamics studies of Kolliphor EL. *J Pharm Sci* 2019;**108**:193–204.
- Qiang F, Lee BJ, Ha I, Kang KW, Woo ER, Han HK. Effect of maceligan on the systemic exposure of paclitaxel: *In vitro* and *in vivo* evaluation. *Eur J Pharmaceut Sci* 2010;**41**:226–31.
- Lee CK, Choi JS. Effects of silibinin, inhibitor of CYP3A4 and P-glycoprotein *in vitro*, on the pharmacokinetics of paclitaxel after oral and intravenous administration in rats. *Pharmacology* 2010;**85**:350–6.
- Paek IB, Ji HY, Kim MS, Lee GS, Lee HS. Simultaneous determination of paclitaxel and a new P-glycoprotein inhibitor HM-30181 in rat plasma by liquid chromatography with tandem mass spectrometry. *J Sep Sci* 2006;**29**:628–34.
- Kong L, Campbell F, Kros A. DePEGylation strategies to increase cancer nanomedicine efficacy. *Nanoscale Horiz* 2019;**4**:378–87.
- Kataoka K, Harada A, Nagasaki Y. Block copolymer micelles for drug delivery: design, characterization and biological significance. *Adv Drug Deliv Rev* 2012;**64**:37–48.
- Yang YQ, Lv YJ, Shen CY, Shi TT, He HS, Qi JP, et al. *In vivo* dissolution of poorly water-soluble drugs: proof of concept based on fluorescence bioimaging. *Acta Pharm Sin B* 2021;**11**:1056–68.
- He HS, Jiang SF, Xie YC, Lu Y, Qi JP, Dong XC, et al. Reassessment of long circulation *via* monitoring of integral polymeric nanoparticles justifies a more accurate understanding. *Nanoscale Horiz* 2018;**3**:397–407.
- Xia F, Chen ZJ, Zhu QG, Qi JP, Dong XC, Zhao WL, et al. Gastrointestinal lipolysis and trans-epithelial transport of SMEDDS *via* oral route. *Acta Pharm Sin B* 2021;**11**:1010–20.
- Xie YK, Shi BK, Xia F, Qi JP, Dong XC, Zhao WL, et al. Epithelia transmembrane transport of orally administered ultrafine drug particles evidenced by environment sensitive fluorophores in cellular and animal studies. *J Control Release* 2018;**270**:65–75.
- Shen CY, Yang YQ, Shen BD, Xie YK, Qi JP, Dong XC, et al. Self-discriminating fluorescent hybrid nanocrystals: efficient and accurate tracking of translocation *via* oral delivery. *Nanoscale* 2018;**10**:436–50.
- Brouwer E, Verweij J, De Bruijn P, Loos WJ, Pillay M, Buijs D, et al. Measurement of fraction unbound paclitaxel in human plasma. *Drug Metab Dispos* 2000;**28**:1141–5.
- He HS, Xie YC, Lv YJ, Qi JP, Dong XC, Zhao WL, et al. Bioimaging of intact polycaprolactone nanoparticles using aggregation-caused quenching probes: size-dependent translocation *via* oral delivery. *Adv Healthcare Mater* 2018;**7**:1800711.
- Xia F, Fan WF, Jiang SF, Ma YH, Lu Y, Qi JP, et al. Size-dependent translocation of nanoemulsions *via* oral delivery. *ACS Appl Mater Interfaces* 2017;**9**:21660–72.
- Kumar R, Sirvi A, Kaur S, Samal SK, Roy S, Sangamwar AT. Polymeric micelles based on amphiphilic oleic acid modified carboxymethyl chitosan for oral drug delivery of BCS class IV compound: intestinal permeability and pharmacokinetic evaluation. *Eur J Pharm Sci* 2020;**153**:105466.
- Ramalingam P, Ko YT. Improved oral delivery of resveratrol from *N*-trimethyl chitosan-*g*-palmitic acid surface-modified solid lipid nanoparticles. *Colloids Surf B* 2016;**139**:52–61.

42. Guo HJ, Zhang DR, Li CY, Jia LJ, Liu GP, Hao LL, et al. Self-assembled nanoparticles based on galactosylated *O*-carboxymethyl chitosan-graft-stearic acid conjugates for delivery of doxorubicin. *Int J Pharm* 2013;**458**:31–8.
43. Yuan H, Lu LJ, Du YZ, Hu FQ. Stearic acid-g-chitosan polymeric micelle for oral drug delivery: *in vitro* transport and *in vivo* absorption. *Mol Pharm* 2011;**8**:225–38.
44. Xiao YL, Li PL, Cheng YN, Zhang XK, Sheng JZ, Wang DC, et al. Enhancing the intestinal absorption of low molecular weight chondroitin sulfate by conjugation with α -linolenic acid and the transport mechanism of the conjugates. *Int J Pharm* 2014;**465**:143–58.
45. Khurana RK, Beg S, Burrow AJ, Vashishta RK, Katare OP, Kaur S, et al. Enhancing biopharmaceutical performance of an anticancer drug by long chain PUFA based self-nanoemulsifying lipidic nanomicellar systems. *Eur J Pharm Biopharm* 2017;**121**:42–60.
46. Kobayashi S, Kondo S, Juni K. Permeability enhancing effect of oleic acid and its mechanism in human alveolar A549 cells. *Eur J Pharmaceut Sci* 1996;**4**:267–72.
47. Komarov PG, Shtil AA, Buckingham LE, Balasubramanian M, Piraner O, Emanuele RM, et al. Inhibition of cytarabine-induced *MDR1* (P-glycoprotein) gene activation in human tumor cells by fatty acid-polyethylene glycol-fatty acid diesters, novel inhibitors of P-glycoprotein function. *Int J Cancer* 1996;**68**:245–50.
48. Lai SK, Suk JS, Pace A, Wang YY, Yang M, Mert O, et al. Drug carrier nanoparticles that penetrate human chronic rhinosinusitis mucus. *Biomaterials* 2011;**32**:6285–90.
49. Dünnhaupt S, Kammona O, Waldner C, Kiparissides C, Bernkop-Schnürch A. Nano-carrier systems: strategies to overcome the mucus gel barrier. *Eur J Pharm Biopharm* 2015;**96**:447–53.
50. Suk JS, Xu QG, Kim NH, Hanes J, Ensign LM. PEGylation as a strategy for improving nanoparticle-based drug and gene delivery. *Adv Drug Deliv Rev* 2016;**99**:28–51.
51. Zaichik S, Steinbring C, Caliskan C, Bernkop-Schnürch A. Development and *in vitro* evaluation of a self-emulsifying drug delivery system (SEDDS) for oral vancomycin administration. *Int J Pharm* 2019;**554**:125–33.
52. Huang YP, Yu Q, Chen ZJ, Wu W, Zhu QG, Lu Y. *In vitro* and *in vivo* correlation for lipid-based formulations: current status and future perspectives. *Acta Pharm Sin B* 2021;**11**:2469–87.
53. Chen TK, He B, Tao JS, He Y, Deng HL, Wang XQ, et al. Application of Förster resonance energy transfer (FRET) technique to elucidate intracellular and *in vivo* biofate of nanomedicines. *Adv Drug Deliv Rev* 2019;**143**:177–205.